Title	Multifunctional Triggering by Solid-Phase Molecular Motion : Relaxor Ferroelectricity, Modulation of Magnetic Exchange Interactions, and Enhancement of Negative Thermal Expansion
Author(s)	Li, Simin; Takahashi, Kiyonori; Huang, Rui-Kang et al.
Citation	Chemistry of materials, 35(6), 2421-2428 https://doi.org/10.1021/acs.chemmater.2c03552
Issue Date	2023-03-08
Doc URL	https://hdl.handle.net/2115/91294
Rights	This document is the Accepted Manuscript version of a Published Work that appeared in final form in Chemistry of materials, copyright c American Chemical Society after peer review and technical editing by the publisher. To access the final edited and published work see https://pubs.acs.org/articlesonrequest/AOR-GCAKW5R4HYHTFXUPX3QT.
Type	journal article
File Information	4ApyB18toACSJournals_rev.pdf

Multifunctional triggering by solid-phase molecular motion: relaxor ferroelectricity, modulation of magnetic exchange interactions, and enhancement of negative thermal expansion

Simin Li,[a] Kiyonori Takahashi,[a,b]* Rui-Kang Huang,[a,b] Chen Xue,[a,b] Kenta Kokado, [a,b,c,d] Norihisa Hoshino,[e] Tomoyuki Akutagawa,[e] Sadafumi Nishihara,[d,f] Takayoshi Nakamura[a,b]*

[a] Research Institute for Electronic Science, Hokkaido University, Sapporo 001-0020, Japan

[b] Graduate School of Environmental Science, Hokkaido University, Sapporo 001-0020, Japan

[c] Toyota Technological Institute, Hisakata, Tempaku-ku, Nagoya, 468-8511, Japan

[d] JST PRESTO, Honcho, Kawaguchi, Saitama 332-0012, Japan

[e] Institute of Multidisciplinary Research for Advanced Materials, Tohoku University, 1-1 Katahira, Aoba-ku, Sendai, Miyagi 980-8577, Japan

[f] Department of Chemistry, Graduate School of Advanced Science and Engineering, Hiroshima University, Higashi-hiroshima, Hiroshima, 739-8527, Japan

KEYWORDS. Multifunctional materials, Supramolecular cation, Molecular motion, Ferroelectricity, Magnetic, Negative thermal expansion

ABSTRACT: Although the development of artificial molecular machines has garnered considerable attention in recent years, the construction of multifunctional solid-state molecular machines still faces several challenges. Herein, we report a supramolecular approach as an efficient strategy for building multifunctional trigger systems. In crystals composed of $[Ni(dmit)_2]^-$ with a spin of S = 1/2 and supramolecular structures consisting of 4-aminopyridinium$^+$ and benzo[18]crown-6, supramolecular cations with dynamic degrees of freedom affect the magnetic and dielectric properties and induce negative thermal expansion (NTE). The supramolecular cations in the crystals form one-dimensional columns. Two adjacent columns form a supramolecular ladder structure *via* π ••• π interactions between the phenylene groups of benzo[18]crown-6, and are arranged within a two-dimensional layer. A disorder between the two sites of the phenylene ring was observed in one of the crystallographically independent benzo[18]crown-6. Disordered benzo[18]crown-6 formed polar domains within the crystal, resulting in relaxor ferroelectricity. With increasing temperature, the supramolecular ladders elongated and the translational motion of the benzo[18]crown-6 caused the molecular ladder to move closer to each other. Consequently, the crystals shrunk in the direction perpendicular to the ladder, exhibiting uniaxial NTE, and the magnetic exchange interaction between the $[Ni(dmit)_2]^-$ crystals was disrupted.

INTRODUCTION

The development of artificial molecular machines based on molecular motion has been actively studied in various fields;[1-7] however, most studies have focused on motion in the liquid phase. Because the molecular motion in the liquid phase is random and incoherent,[7] it is difficult to determine the directionality of isotropic mechanical motion. Molecules in the crystalline state generally have tightly packed and ordered structures, leaving insufficient space for molecular motion. However, if sufficient space is created in the solid, molecular motion and reorientation become possible, which are the basis for the development of multifunctional molecular machines in the crystalline state.[6-10]

It is well known that the introduction of supramolecular cations into molecular crystals can result in solid-state dynamic molecular systems.[9-12] For instance, 180° flip-flop motion of *m*-fluoroanilinium$^+$ has been observed in the crystals of (*m*-fluoroanilinium$^+$)(dibenzo[18]crown-6)$[Ni(dmit)_2]^-$ ($dmit^{2-}$ = 2-thioxo-1,3-dithiole-4,5-dithiolate). The *m*-fluoroanilinium$^+$ rotations are correlated with each other, resulting in ferroelectricity owing to dipole inversion induced by the outer electric field.[9]

Furthermore, supramolecular cations with dynamic degrees of freedom can modulate the magnetic exchange interaction (J) between magnetic $[Ni(dmit)_2]^-$ with a spin of $S = 1/2$.[10-13] Notably, the magnetic behavior of the $[Ni(dmit)_2]^-$ dimer is significantly influenced by the rotation of [18]crown-6 in Cs_2([18]crown-6)$_3$ in $(Cs^+)_2$([18]crown-6)$_3[Ni(dmit)_2]^-{}_2$.[12]

We recently reported that one-dimensional (1D) chain structures formed by hydrogen bonds are also useful for realizing molecular motion in crystals.[14-16] For instance, in $[Cu^{II}(3,4\text{-difuluorobenzoate})_2(\text{pyridine})_2(H_2O)]$, penta-coordinated mononuclear copper (II) complexes are linked by O-H•••O hydrogen bonds to form 1D chains. The dynamic motion of fluorobenzoate ligands was observed as a change in the dielectric constant.[14] In (4,4'-bipyridinium)(dibenzo[24]crown-8)$[Ni(dmit)_2]^-$, monoprotonated 4,4-bipyridinium forms a 1D chain through hydrogen bonding. This 1D chain forms a pseudo-polyrotaxane structure with dibenzo[24]crown-8. One of the pyridyl rings of 4,4-bipyridinium was isolated from the other molecules; it exhibited rotational motion.[15] Combining the supramolecular approach with hydrogen-bonded 1D chain structures is expected to be a new supramolecular approach for the construction of multifunctional materials using molecular motion in the solid state.

Despite the effectiveness of supramolecular approaches in realizing solid-phase molecular motion, dynamic molecular systems that simultaneously exhibit pronounced dielectric and magnetic responses are still rare. In this study, a supramolecular structure consisting of 4-aminopyridinium$^+$ (4-ApyH$^+$) and benzo[18]crown-6 (B[18]crown-6) was introduced into [Ni(dmit)$_2$]$^-$ salt. Both -NH$_2$ and pyridinium N$^+$-H groups of 4-ApyH$^+$ can form hydrogen bonds with the [18]crown-6 derivative. Therefore, 1D assemblies of supramolecular cations were formed in the crystal. B[18]crown-6 exhibited molecular polarization derived from the phenylene group, which fluctuates in the 1D chain and was observed as a dielectric anomaly. Supramolecular fluctuations in the flexible hydrogen-bonded chains caused a negative thermal expansion (NTE) of the crystals and perturbed the magnetic exchange interaction by affecting the overlap in [Ni(dmit)$_2$]$^-$. (4-ApyH$^+$)(B[18]crown-6)[Ni(dmit)$_2$]$^-$ (**1**) is a multifunctional trigger system in which the molecular degrees of freedom in the supramolecular cation affect the magnetic and dielectric properties and cause NTE.

RESULTS AND DISCUSSION

The introduction of a supramolecular cation consisting of 4-ApyH$^+$ and B[18]crown-6 into the [Ni(dmit)$_2$]$^-$ salt resulted in (4-ApyH$^+$)(B[18]crown-6)[Ni(dmit)$_2$]$^-$ crystals (**1**) in the *P*-1 space group. The packing structure of crystal **1** at 177 K is shown in Figure 1a. For the [Ni(dmit)$_2$]$^-$, 4-ApyH$^+$, and B[18]crown-6 molecules, each of them has two configurations that are crystallographically independent in the asymmetric unit (Figure S1a), and are denoted as **dm1**, **dm2**, **Ap1**, **Ap2**, **CE1**, and **CE2**, respectively. 4-ApyH$^+$ and B[18]crown-6 molecules are alternately arranged along the *a*-axis in the order of **Ap1**, **CE1**, **Ap2**, and **CE2**, forming a 1D array of supramolecular cations with the minimal motif [**•••Ap1•••CE1•••Ap2•••CE2•••**] (Figure 1b).

The centers of the two pyridyl N atoms and two amino N atoms of the adjacent 4-ApyH$^+$ are denoted as **A** and **B**, respectively (Figure 1b). If the centers of **•••A•••B•••A•••B•••** are continuously connected along the *a*-axis, the 1D stacking of the supramolecular cations is considered a zigzag pattern. Because 4-ApyH$^+$ is arranged head-to-head and tail-to-tail in the supramolecular column, **CE1** and **CE2** interact with the pyridyl N-H$^+$ and amino -NH$_2$ groups of 4-ApyH$^+$, respectively, through hydrogen bonds (further details are illustrated in Figure S4 and listed in Table S2). Stronger hydrogen bonds were observed when the donor or acceptor site of the hydrogen bond had a positive or negative charge.[17] Thus, **CE1** formed stronger N-H$^+$•••O hydrogen bonds with the two nearest 4-ApyH$^+$ cations, whereas **CE2** formed weaker N-H•••O hydrogen bonds than those around **CE1**. Two adjacent supramolecular columns formed a supramolecular ladder structure *via* C-H•••π interactions (3.591 – 3.672 Å) and π•••π interactions (3.696 – 3.929 Å, 0°) between **CE1** molecules (light blue backgrounds in Figure 1).

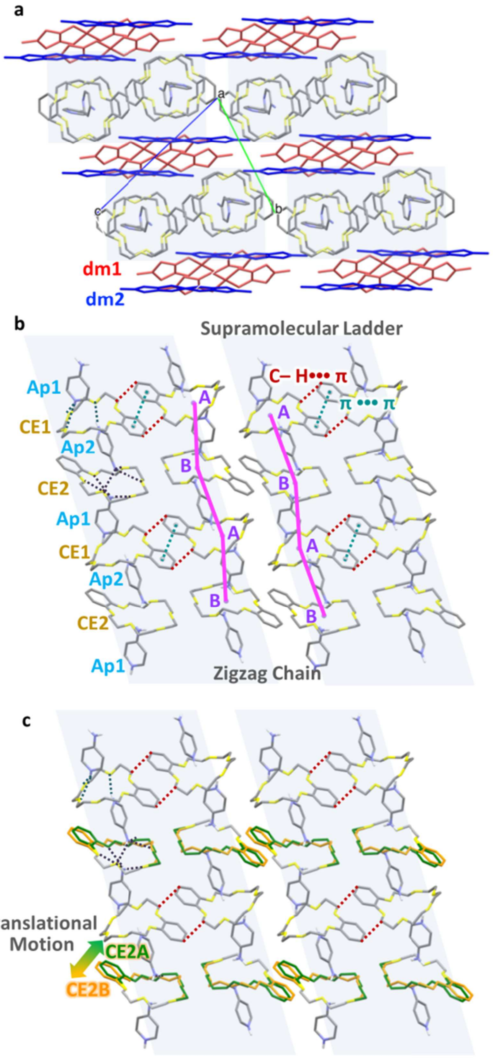

Figure 1. Crystal structure of **1**. The C, H, N, and O atoms in 4-ApyH$^+$ and B[18]crown-6 are depicted in gray, white, blue, and yellow, respectively. All molecules are depicted as capped rod models. Hydrogen atoms are omitted for clarity, except for those involved in hydrogen bonds in (b) and (c). The light blue background represents the supramolecular ladder. (a) Packing structure at 177 K viewed along the *a*-axis. Two crystallographically independent [Ni(dmit)$_2$]$^-$ are marked with red and blue. (b, c) Supramolecular structures at (b) 108 K and (c) 381 K in the *bc* plane. Disordered parts of B[18]crown-6 in (c) are shown in orange and green. The gray balls in (b) indicate the planar center of the phenylene ring. The purple balls in (b) indicate the centers of the N atoms of the adjacent 4-ApyH$^+$ cations, denoted as **A** (between two pyridyl N atoms) and **B** (between two amino N atoms), respectively. The magenta lines connecting **A** and **B** are visual guides. The C-H•••π and π•••π interactions between **CE1** are shown as dashed red and cyan lines, respectively. The brown dashed line represents the N-H•••O hydrogen bond between the -NH$_2$ group of 4-ApyH$^+$ and the O atom of B[18]crown-6. The N-H$^+$•••O hydrogen bond between the pyridine N-H$^+$ and the O atom of B[18]crown-6 is indicated by the blue dashed line.

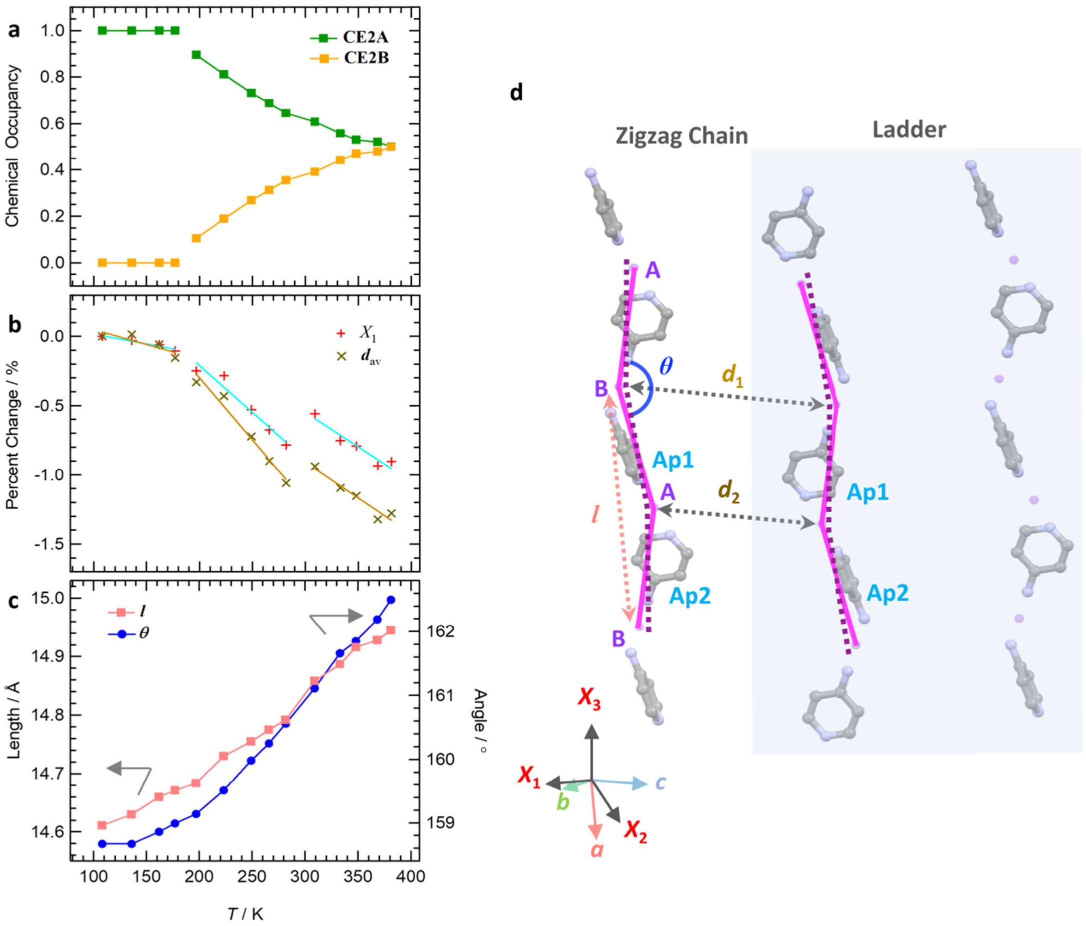

Figure 2. (a) Temperature dependence of **CE2** occupancy, with **CE2A** and **CE2B** occupancies shown in green and orange, respectively. (b) Percent change in X_1 and inter-ladder distance ($\boldsymbol{d}_{\mathbf{av}}$, see text) versus temperature. The bright blue and brown lines are linear fits of X_1 and $\boldsymbol{d}_{\mathbf{av}}$, respectively. (c) Temperature dependence of the length (***l***, left axis) and angle (θ, right axis) of the zigzag chain. (d) Simplified zigzag chain. The magenta lines represent zigzag chains at 108 K as shown in Figure 1b. The purple dotted lines indicate zigzag chains at 381 K. The light red and gray dashed lines represent zigzag chain length (***l***) and distance ($\boldsymbol{d}_\mathbf{1}$ and $\boldsymbol{d}_\mathbf{2}$), respectively. The blue arc line shows the zigzag chain angle (θ).

No significant interactions were observed between adjacent **CE2**s, in contrast to what was observed between **CE1** molecules within the ladders. The supramolecular ladders were arranged parallel to the *bc* plane to form two-dimensional (2D) arrays. Between the 2D layers of supramolecular cations, **dm1** and **dm2** formed dimers, which were aligned in the *bc* plane to form a 2D layer of $[Ni(dmit)_2]^-$. The 2D layers of supramolecular cations and $[Ni(dmit)_2]^-$ were stacked alternately in the [011] direction (Figure 1a). In addition, the single-crystal structure was determined in the temperature range of 108 – 381 K, approximately every 20 K. The overall structure of **1** did not change with increasing temperature. **Ap1** and **Ap2** remained ordered even at higher temperatures owing to hydrogen bonding, and **CE1** also exhibited no disorder. In contrast, **CE2** exhibited orientational disorder over two sites at temperatures higher than 177 K. There is almost no intermolecular interaction between neighboring **CE2** molecules across the ladder, allowing translational motion of the phenylene ring of **CE2** within the crystal (Figure 1c). The two disordered sites of **CE2**, denoted as **CE2A** and **CE2B**, are shown in Figure 1c in green and orange, respectively. With the increase in temperature from 177 K, the occupancy of **CE2A** steadily decreases, reaching 0.8958 at 197 K and 0.5 at 381 K, indicating translational motion of the phenylene group within the crystal (Figure 2a).

Figure S5 illustrates the temperature dependence of unit cell parameters. In general, the lattice length increases with increasing temperature because the vibrations of the atoms increase and become more anharmonic, whereas the intermolecular interactions weaken as the temperature increases.[18,19] Notably, the length of the *b*-axis is almost unchanged with temperature. Because the crystalline system is triclinic with non-orthogonal unit cell axes, the principal axes were used to evaluate the linear expansion coefficients.[20] PASCal software was used to determine the thermal expansion with increasing temperature. The principal axes were labeled as X_1, X_2, and X_3, respectively, where the orientation of the principal axes relative to the unit cell axes was $X_1 = -0.0402a + 0.9038b - 0.4262c$, $X_2 = 0.6995a + 0.1818b + 0.6912c$, and $X_3 = -0.8542a + 0.3353b + 0.3974c$ (Table S3). The percentage change in X_1 length with increasing temperature is shown in Figure 2b (those of X_2 and X_3 are shown in Figure S6). X_2 and X_3 monotonically increase with the increase in temperature from 108 to 381 K. The coefficients of linear thermal expansion (CLTE) for X_2 and X_3 are 76.9 × 10^{-6} K^{-1} and 103.7 × 10^{-6} K^{-1}, respectively. In contrast, the CLTE of X_1 is −14.3 × 10^{-6} K^{-1} in the temperature range of 108–177 K, −72.1 × 10^{-6} K^{-1} in the temperature range of 197–282 K, and −50.8 × 10^{-6} K^{-1} in the temperature range of 309–381 K (Figure 2b and Tables S4, S5, and S6). Uniaxial NTE in the X_1 direction was confirmed. The CLTE for X_1 increased in absolute value by a factor of 5.03 from 197 to 282 K, and by a factor of 3.55 at temperatures higher than 309 K, compared with values at temperatures lower than 177 K. In general, NTE is entropy-driven, and entropy can be acquired through molecular motion in the crystals.[21-24] Translational motion of **CE2** is initiated at a temperature range of 177–197 K, meaning that the increase in NTE can be attributed to **CE2** motion. A linear fit of the temperature variation of **CE2A** occupancy was observed to be −3.28 × 10^{-3} K^{-1} in a temperature range of 177–282 K and −1.43 × 10^{-3} K^{-1} in a temperature range of 309–381 K, which roughly correlates with the absolute values of CLTE. The decrease in CLTE at temperatures higher than 309 K is likely due to the decrease in the rate of occupancy change for **CE2A**.

To clarify the origin of NTE at the molecular level, we focused on the zigzag chain length ($\boldsymbol{l}$, the length between two adjacent **B** points, is equal to that of two adjacent **A** points), zigzag chain angle ($\boldsymbol{\theta}$, ∠ABA = ∠BAB = $\boldsymbol{\theta}$), and zigzag chain distances between supramolecular ladders ($\boldsymbol{d_1}$ and $\boldsymbol{d_2}$) (Figures 2d and Table S7). The contribution of the *a*-axis to X_1 is negligible; however, it is significant for X_2 and X_3. In particular, the *a*-axis contribution was dominant for X_3. As shown in Figure 1a, the *a*-axis coincides with the stacking direction of the supramolecular cations, which is also the direction of the elongation of the zigzag chains. Thus, X_1 lies almost in the plane of the supramolecular ladder arrangement, whereas X_3 is relatively oriented in the direction of elongation of the zigzag chain (Figure 2d).

The $\boldsymbol{l}$ and $\boldsymbol{\theta}$ of the zigzag chains increased with increasing temperature (14.611 Å and 158.67° at 108 K, increasing to 14.945 Å and 162.5° at 381 K, respectively), resulting in the positive thermal expansion of X_2 and X_3 (Figure 2c). In particular, X_3, which was aligned in the zigzag chain direction, exhibited a relatively large positive CLTE. Because the zigzag chains are elongated and the phenylene group of CE2 between the supramolecular ladders undergoes translational motion, the supramolecular ladders are closer to each other, and NTE is induced along the direction of the supramolecular ladder alignment (X_1). To quantify the distance between ladders, the average value ($\boldsymbol{d}_{\mathbf{av}}$) of the distances between points A–A and B–B on adjacent ladders (denoted as $\boldsymbol{d_1}$ and $\boldsymbol{d_2}$, respectively, in Figure 2d) was plotted as a function of temperature (Figure 2b). The change in $\boldsymbol{d}_{\mathbf{av}}$ with temperature ($\Delta\boldsymbol{d}_{\mathbf{av}}/T$) was −2.25 × 10^{-3}, −6.97 × 10^{-3}, and −4.71 × 10^{-3} K^{-1} in the temperature ranges of 108–177, 197–282, and 309–381 K, respectively. The trend in $\Delta\boldsymbol{d}_{\mathbf{av}}/T$ corresponds to the rate of change in the occupancy rate of **CE2A** and the temperature change in the CLTE of X_1. The disorder of **CE2** molecules with increase in temperature causes packing rearrangement of the zigzag chains, and as the zigzag chains elongate, the crystal shrinks in the direction perpendicular to the zigzag chains. Consequently, a uniaxial NTE along the principal axis of X_1 was observed. The contraction along X_1 was based on supramolecular rearrangements in the direction perpendicular to the zigzag chains.

The molecular motion in crystals affects their dielectric properties. The temperature and frequency dependences of the dielectric constant were measured for single crystals of **1** with alternating electric fields applied almost in the directions of the *a*-, *b*-, and *c*-axes. The temperature and frequency dependence of the real part of the dielectric constant (ε_1) along the *b*-axis (associated with the translational motion of B[18]crown-6) is shown in Figure 3a (see Figure S9 for the temperature and frequency dependences of ε_1 along the *a*- and *c*-axes). In the low-temperature range (90-160 K), ε_1 slightly changed at all frequencies. Above 160 K, ε_1 increased, near the onset temperature of **CE2** disordering. With increasing temperature, the change in ε_1 exhibits a broad peak. Arrhenius plot (measured frequency (*f*) *versus* inverse temperature (T^{-1}) for peak tops) follows the Vogel–Fulcher law: $f = f_0 \exp\{-U/[k_B(T-T_f)]\}$, with the parameters of U = 54.3 kJ mol^{-1}, pre-exponential factor of f_0 = 4710 Hz, freezing temperature of T_f = 298 K, and Boltzmann constant of k_B (Figure S8).

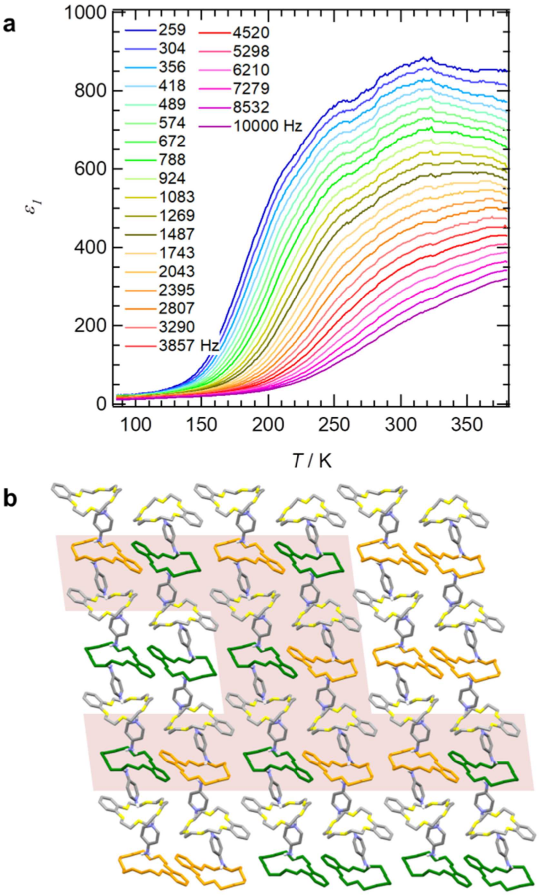

Figure 3. (a) Temperature and frequency dependence of the real part of the dielectric constant (ε_1) along the *b*-axis. (b) Schematic view of polar nanodomains in 2D B[16]crown-6 layer. Green and orange molecules indicate **CE2A** and **CE2B**, respectively. Polar regions are shown on a light red background consisting of **CE2A** – **CE2B** pairs.

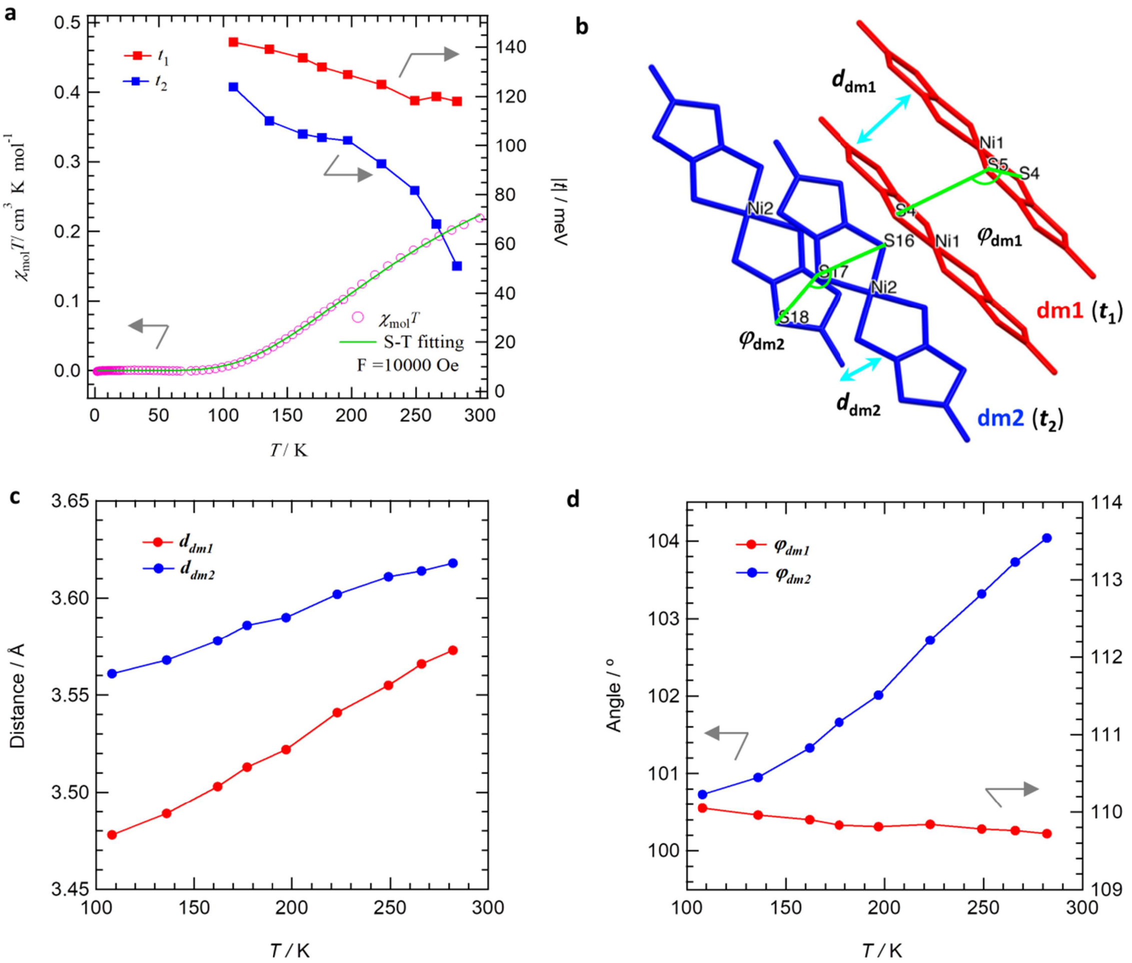

Figure 4. (a) Temperature dependence of χ_mT (right axis) and transfer integrals (left axis). The green line indicates the fit by the singlet – triplet thermal excitation (S – T) model with the temperature-dependent *J* (see text). (b) Two types of dimers formed in the crystal. Dimers consisting of **dm1** and **dm2** are shown in red and blue, respectively. The interplanar distance of $[Ni(dmit)_2]^-$ in the dimer ($\boldsymbol{d}_{\mathbf{dm1}}$ and $\boldsymbol{d}_{\mathbf{dm2}}$) is indicated by light blue arrows. The dihedral angle, a measure of the short-axis slip of the $[Ni(dmit)_2]^-$ dimer, is defined as the angle formed by S4-S5-S4 and S16-S17-S18 ($\boldsymbol{\varphi}_{\mathbf{dm1}}$ and $\boldsymbol{\varphi}_{\mathbf{dm2}}$, respectively), and is shown in green. (c) Temperature dependences of $\boldsymbol{d}_{\mathbf{dm1}}$ and $\boldsymbol{d}_{\mathbf{dm2}}$. (d) Temperature dependences of $\boldsymbol{\varphi}_{\mathbf{dm1}}$ and $\boldsymbol{\varphi}_{\mathbf{dm2}}$.

No clear peaks in the temperature and frequency dependence of ε_1 were observed when alternating electric fields were applied along the *a*- or *c*-axis (Figure S9). These results indicate that the dielectric response is associated with the translational motion of B[18]crown-6. The relatively large ε_1 and frequency-dependent broad peaks observed in the *b*-axis dielectric response are similar to those of relaxor ferroelectrics.[25-27] To confirm the relaxor ferroelectricity, an electric field was applied along the polarization axis (the *b*-axis of the single crystal sample), and the electric field polarization curve was measured at 50 K. The residual polarization without the linear dielectric loss component shows a hysteresis loop with inflection points (Figure S10). The obtained hysteresis curves, coercive field, and polarization value are comparable to those of ferroelectric hysteresis reported in previous studies on molecular-based ferroelectrics.[28-30] Crystal **1** shows relaxor ferroelectricity.

Although the compound crystallizes in nonpolar space groups, B[18]crown-6 with **CE2A** or **CE2B** conformations can be assembled to form polar nanodomains with a ferroelectric order in the crystal (Figure 3b). The presence of short-range order breaks the average symmetry of the crystal, and the crystal behaves similarly to a relaxor ferroelectric.

To evaluate the stabilization energies of the B[18]crown-6 pairs adjacent to each other across the ladder of supramolecular cations, the coordinates of **CE2A-CE2A**, **CE2B-CE2B**, and **CE2A-CE2B** at 277 K were extracted, and the stabilization energy of each pair was determined through DFT calculations (counterpoise-corrected B3LYP-D3/6-31G(d,p) level). Because the **CE2A-CE2A** and **CE2B-CE2B** pairs are related by inverted centers, the polarization vectors cancel each other. In contrast, the **CE2A-CE2B** combination has a dipole moment of 0.9 Debye, resulting in a finite polarization. The complexation energies of each pair were determined as –4.37, –6.70, and –5.52 kcal mol^{-1} for **CE2A-CE2A**, **CE2B-CE2B**, and **CE2A-CE2B**, respectively. This energy difference is comparable to the temperature at which a large dielectric response is observed. Disruption of **CE2** generates polar nanodomains composed of a combination of

CE2A and **CE2B** in the crystal, resulting in relaxor ferroelectricity.

Supramolecular cations with dynamic degrees of freedom also modulate the magnetic exchange between $[\mathrm{Ni(dmit)_2}]^-$ anions. The temperature dependence of the molar magnetic susceptibilities (χ_m) is shown as $\chi_\mathrm{m}T$ *versus* T plot in Figure 4a. $[\mathrm{Ni(dmit)_2}]^-$ exhibits relatively strong antiferromagnetic interactions, even near room temperature. In the crystal, two crystallographically independent $[\mathrm{Ni(dmit)_2}]^-$ anions (marked by **dm1** and **dm2** in Figure 1a) are strongly dimerized with the corresponding intradimer transfer integrals t_1 and t_2 of 118.00 and 50.98 meV at 282 K, respectively (Figures 4a). Because the magnitude of J is proportional to the square of the transfer integral (t),[31-33] a large t within the dimer suggests that the magnetic behavior of the crystal is dominated by the J between the dimers. Therefore, we decided to apply the singlet – triplet thermal excitation (S-T) model to reproduce the temperature dependence of $\chi_\mathrm{m}T$ for crystal **1** using the Landé g-factor 2.042 obtained from the EPR spectra (Figure S11). However, the experimental data could not be fitted to the model with constant J (Figure S12).

We applied a modified S-T model in which J depends on temperature, and succeeded in reproducing the experimental results of $\chi_\mathrm{m}T$. The temperature dependence of $\chi_\mathrm{m}T$ agrees well with the modified S-T model with g = 2.042 and $J/k_\mathrm{B} = 0.32\ T - 303.42$ (Figure 4a, left axis). This J trend corresponds to the temperature dependence of t in the intradimer. The temperature dependences of t_1 and t_2 were evaluated from the coordinates of the $[\mathrm{Ni(dmit)_2}]^-$ dimer at different temperatures, and are summarized in Figure 4a (right axis). Both t_1 and t_2 increased with decreasing temperature to 142.03 and 123.82 meV at 108 K, respectively.

Decreases in t_1 and t_2 with increasing temperature were due to the relative conformational change of $[\mathrm{Ni(dmit)_2}]^-$ in the dimer. We plotted the temperature dependence of the interplanar distance between $[\mathrm{Ni(dmit)_2}]^-$ in each dimer ($\boldsymbol{d}_\mathbf{dm1}$ and $\boldsymbol{d}_\mathbf{dm2}$) in addition to the dihedral angles ($\boldsymbol{\varphi}_\mathbf{dm1}$ and $\boldsymbol{\varphi}_\mathbf{dm2}$) determined as the angle formed by three sulfur atoms of the $[\mathrm{Ni(dmit)_2}]^-$ dimer (S4-S5-S4 and S16-S17-S18 in Figure 4b). In both dimers, the interplanar distances of $\boldsymbol{d}_{dm1}$ and $\boldsymbol{d}_\mathbf{dm2}$ increased with increasing temperature (Figure 4c), resulting in a decrease in J within the dimer. In addition, $\boldsymbol{\varphi}_\mathbf{dm}$, a measure of the short-axis slip of the $[\mathrm{Ni(dmit)_2}]^-$ dimer, changed more significantly with increasing temperature for **dm2**, resulting in a more attenuated t_2 than t_1 (Figure 4d). The conformational change of the supramolecular cation perturbed the through-space interaction of the singly occupied molecular orbital of $[\mathrm{Ni(dmit)_2}]^-$, thereby affecting the magnetic behavior of the crystal.

CONCLUSION

We reported a multifunctional trigger system for $(\text{4-ApyH}^+)(\text{B[18]crown-6})[\mathrm{Ni(dmit)_2}]^-$. The supramolecular structure composed of B[18]crown-6 and 4-ApyH$^+$ formed a ladder structure in the crystal. Pairs of B[18]crown-6 with disordered phenylene rings formed polar domains, and these fluctuations caused relaxor ferroelectric-like dielectric responses. The disorder of B[18]crown-6 with increasing temperature modulated the supramolecular structure, and the crystals exhibited NTE perpendicular to the supramolecular ladder and further perturbed the magnetic exchange interaction in $[\mathrm{Ni(dmit)_2}]^-$. The design principle of the multifunctional trigger system proposed in this study provides opportunities for the development of functional materials based on artificial molecular machines.

Experimental

General

All the reagents were used without further purification. Elemental analyses were performed using a CHN analyzer (CE440, Exeter Analytical, Inc.) at the Instrumental Analysis Division, Equipped Management Center, Creative Research Institution, Hokkaido University.

Crystal Preparation

Precursors of $(\mathrm{TBA}^+)[\mathrm{Ni(dmit)_2}]^-$ (TBA = tetra-*n*-butylammonium) and $(\text{4-ApyH}^+)(\mathrm{BF_4})$ were prepared according to previously reported methods.[34,35] Crystals of **1** were obtained through natural evaporation. $(\text{4-ApyH}^+)(\mathrm{BF_4})$ (54.88 mg, 0.30 mmol), B[18]crown-6 (140.56 mg, 0.45 mmol), and $(\mathrm{TBA}^+)[\mathrm{Ni(dmit)_2}]^-$ (103.79 mg, 0.15 mmol) were dissolved in acetonitrile, and $(\text{4-ApyH}^+)(\text{B[18]crown-6})[\mathrm{Ni(dmit)_2}]$ (**1**) was obtained as black block crystals (94.32 mg, 73.21% yield). The theoretical and experimental compositions (%) of crystal **1** ($\mathrm{C_{27}H_{31}N_2NiO_6S_{10}}$) were C 37.76, H 3.64, N 3.26, and C 37.74, H 3.54, N 3.18, respectively. The structures were determined using elemental and X-ray analyses. The crystal data, data collection, and reduction parameters of crystal **1** at various temperatures are listed in Table S1. The powder X-ray diffraction (PXRD) pattern of the polycrystalline sample of **1** was in good agreement with those simulated using single-crystal analysis, verifying the purity (Figure S2). The thermogravimetric (TG) measurements are shown in Figure S3.

Crystal Structure Determination

Temperature-dependent structural analysis of the single crystals was performed using a Rigaku XtaLAB synergy diffractometer with a single microfocus $\mathrm{Mo_{K\alpha}}$ X-ray radiation source (PhotonJet-S) equipped with a hybrid pixel (HyPix) array detector (HyPix-6000HE). Multiscan absorption corrections were applied to the reflection data. A single crystal was mounted on a mounted CryoLoop (Hampton Research) with Paratone 8277 (Hampton Research). Temperature dependence was measured for the same crystal. Data collection, cell refinement, and data reduction were performed using *CrysAlisPRO* (Rigaku Oxford Diffraction, 2017). The initial structure was solved using SHELXT,[36] and structural refinement was performed by full-matrix least-squares techniques on F^2 using OLEX2 software.[37] Anisotropic refinement was applied to all atoms except for hydrogen atoms. These data are provided free of charge by the Cambridge Crystallographic Data Centre (CCDC No. 2183639, 2183640, 2183651, 2183652, 2183641, 2183647, 2183642, 2183646, 2183643, 2183644, 2183645, 2183649, 2183650, 2183648, for the structure at the temperatures of 108, 136, 162, 177, 197, 223, 249, 266, 282, 309, 333, 348, 368, and 381 K, respectively).

Dielectric and Polarization Measurements

Temperature- and frequency-dependent dielectric constants were measured using an impedance analyzer 4294A (Agilent) using the four-probe AC impedance method at a frequency range of $10^2 - 10^4$ Hz with about $10^{0.05}$ Hz increments. The ferroelectric hysteresis curve was obtained using a ferroelectric tester (Multiferroic II, Radiant Technologies) at the temperature at 50 K and frequency of 0.1 Hz by remnant hysteresis measurement. The temperature was controlled using cryostats with temperature controller models 331 or 335 (Lake Shore Cryotronics Inc.). Electrical contacts were prepared using a gold paste to attach the 10 μm ϕ gold wires to the single crystals.

Magnetic Measurements

The temperature-dependent magnetic susceptibilities were measured using a Quantum Design MPMS3 SQUID magnetometer in a temperature range of 2 – 300 K. A magnetic field of 1 T was applied for all the temperature-dependent measurements. Prior to sample measurements, measurements under similar conditions were performed on the sample holder (wrap), and their results were directly subtracted from the obtained sample data. In addition to the paramagnetic impurity (Curie constant 6.16×10^{-3} cm^3 K mol^{-1}), which follows the Curie law, a temperature-independent diamagnetic component -4.50×10^{-4} cm^3 mol^{-1} was also subtracted from the obtained data.[38]

Electron spin resonance (ESR)

ESR spectra were measured using a JEOL JES FA-100 spectrometer at room temperature. The single crystals were mounted on the support of a quartz sample holder.

Theoretical Calculations

Transfer integral (*t*): The extended Hückel molecular orbital method within the tight-binding approximation was applied to determine the transfer integrals (*t*) between [Ni(dmit)$_2$] anions. The lowest-unoccupied molecular orbital of the [Ni(dmit)$_2$] molecule was used as the basis function.[39] According to previous studies, semiempirical parameters for Slater-type atomic orbitals were obtained.[39] The *t* values between each pair of molecules were assumed to be proportional to the overlap integral (*S*) according to the equation $t = -10\ S$ eV.

Determination of CTLE

Complexation energy: Complexation energy based on intermolecular interactions was obtained by subtracting the energy of each individual molecule from the energy of the complex. From the atomic positions estimated from single-crystal X-ray structure analysis results at 277 K, we extracted six different molecular cluster pairs (**CE2A-CE2A**, **CE2B-CE2B**, and **CE2A-CE2B**; Figure 1) of B[18]crown-6 (**CE2**) disordered into two sites. The intermolecular interactions of the B[18]crown-6 dimer were estimated from single-point computations at the B3LYP/6-31G(d,p) level.[40,41] Grimme's D3 dispersion model was used for dispersion correction.[42] Computations were performed using the GAUSSIAN16 code set. To remove errors due to the overestimation of stabilization energy (basis set superposition error), the counterpoise correction implemented in GAUSSIAN16 was applied.[43]

ASSOCIATED CONTENT

The Supporting Information is available free of charge at @@@ Crystallographic data, PXRD patterns, TG-DTA curves, PASCal calculations, dielectric results, ESR spectra, magnetic measurements, and their analysis.

AUTHOR INFORMATION

Corresponding Author

* ktakahashi@es.hokudai.ac.jp; tnaka@es.hokudai.ac.jp

Funding Sources

This study was financially supported by JSPS KAKENHI (grant no. JP22H00311 and JP21K14691), JST-PRESTO (grant no. JPMJPR19L3), JSPS Joint Research Projects under the Bilateral Programs (grant no. 120197402), “Dynamic Alliance for Open Innovation Bridging Human, Environment and Materials”, and the Research Program of “Network Joint Research Center for Materials and Devices: Dynamic Alliance for Open Innovation Bridging Human, Environment and Materials” from the Ministry of Education, Culture, Sports, Science and Technology of Japan (MEXT). This research was also financially supported by Murata Science Foundation, Iketani Science and Technology Foundation, and Harmonic Ito Foundation.

ACKNOWLEDGMENT

We thank Ms. Ai Tokumitsu of the Global Facility Center, Hokkaido University, for elemental analysis, and Dr. Shuhei Fukuoka and Dr. Satoaki Matsunaga of the Faculty of Science, Hokkaido University, for χ_m measurements. We also thank Prof. Motohiro Nakano of Osaka University for the fruitful discussion of temperature-dependent magnetic susceptibility.

ABBREVIATIONS

dmit, 2-thioxo-1,3-dithiole-4,5-dithiolate; TBA, tetra-n-butylammonium; 4-ApyH$^+$, 4-aminopyridinium$^+$; B[18]crown-6, benzo[18]crown-6; 1D, one-dimensional; 2D, two-dimensional; NTE, negative thermal expansion; CLTE, coefficient of linear thermal expansion; ε_1, real part of the dielectric constant; E_a, activation energy; χ_m, molar magnetic susceptibilities; *t*, transfer integral; S-T model, singlet-triplet thermal excitation model.

REFERENCES

(1) Schliwa, M.; Woehlke, G.; Molecular motors. *Nature*, **2003**, 422, 759-765.

(2) Credi, A.; Silvi, S.; Venturi, M.; *Molecular Machines and Motors*. Eds. Springer: Heidelberg, Germany, **2014**.

(3) Akutagawa, T.; Nakamura, T.; Supramolecular approach for solid state Brownian rotators. *Dalton Trans*., **2008**, 45, 6335-6345.

(4) Kay, E. R.; Leigh, D. A.; Zerbetto, F.; Synthetic Molecular Motors and Mechanical Machines. *Angew. Chem., Int. Ed.,* **2007**, 46, 72-191.

(5) Kassem, S.; Leeuwen, T. V.; Lubbe, A. S.; Wilson, M. R.; Feringa, B. L.; Leigh, D. A.; Artificial molecular motors. *Chem. Soc. Rev.*, **2017**, 46, 2592-2621.

(6) Khuong, T.-A. V.; Nuñez, J. E.; Godinez, C. E.; Garcia-Garibay, M. A.; Crystalline Molecular Machines: A Quest Toward Solid-State Dynamics and Function. *Acc. Chem. Res*., **2006**, 39, 413-422.

(7) M.-Bulit, P.; Stirk, A. J.; Loeb, S. J.; Rotors, Motors, and Machines Inside Metal – Organic Frameworks. *Trends in Chem*., **2019**, 1, 588-600.

(8) Harada, J.; Ohtani, M.; Takahashi, Y.; Inabe, T.; Molecular Motion, Dielectric Response, and Phase Transition of Charge-Transfer Crystals: Acquired Dynamic and Dielectric Properties of Polar Molecules in Crystals. *J. Am. Chem. Soc*., **2015**, 137, 4477-4486.

(9) Akutagawa, T.; Koshinaka, H.; Sato, D.; Takeda, S.; Noro, S.-I.; Takahashi, H.; Kumai, R.; Tokura, Y.; Nakamura, T.; Ferroelectricity and polarity control in solid-state flip-flop supramolecular rotators. *Nature Mater*., **2009**, 8, 342-347.

(10) Nishihara, S.; Akutagawa, T.; Sato, D.; Takeda, A.; Noro, S.-I.; Nakamura, T.; Multirotations of (Anilinium)([18]Crown-6) Supramolecular Cation

Structure in Magnetic Salt of [Ni(dmit)$_2$]$^-$. *Chem. Asian, J.*, **2007**, 2, 1083-1090.

(11) Nakamura, T.; Akutagawa, T.; Honda, K.; Underhill, A. E.; Coomber, A. T.; Friend, R. H.; A molecular metal with ion-conducting channels. *Nature*, **1998**, 394, 159-162.

(12) Akutagawa, T.; Shitagami, K.; Nishihara, S.; Takeda, S.; Hasegawa, T.; Nakamura, T.; Hosokoshi, Y.; Inoue, K.; Ikeuchi, S.; Miyazaki, Y.; saito, K.; Molecular Rotor of Cs$_2$([18]crown-6)$_3$ in the Solid State Coupled with the Magnetism of [Ni(dmit)$_2$]. *J. Am. Chem. Soc.*, **2005**, 127, 4397-4402.

(13) Nishihara, S.; Akutagawa, T.; Hasegawa, T.; Nakamura, T.; Formation of a molecular spin ladder induced by a supramolecular cation structure. *Chem. Commun.*, **2002**, 408-409.

(14) Takahashi, K.; Miyazaki, Y.; Noro, S.-I.; Nakano, M.; Nakamura, T.; Akutagawa, T.; Dipole fluctuation and structural phase transition in hydrogen-bonding molecular assemblies of mononuclear Cu^{II} complexes with polar fluorobenzoate ligands. *Dalton Trans.*, **2021**, 50, 13680-13685.

(15) Shirakawa, Y.; Takahashi, K.; Sato, H.; Hoshino, N.; Anetai, H.; Noro, S.-I.; Akutagawa, T.; Nakamura, T.; Hydrogen-Bonded Polyrotaxane Cation Structure in Nickel Dithiolate Anion Radical Salts: Ferromagnetic and Semiconducting Behavior Associated with Structural Phase Transition. *Chem. Eur. J.*, **2019**, 25, 6920-6927.

(16) Li, S.; Takahashi, K.; Hisaki, I.; Kokado, K.; Nakamura, T.; One-dimensional DABCO hydrogen-bonding chain in a hexagonal channel of magnetic [Ni(dmit)$_2$]. *Dalton Trans.*, **2020**, 49, 16772-16777.

(17) Jeffery, G.A.; Introduction to hydrogen bonding, oxford university press, **1994**.

(18) Liu, Z.; Gao, Q.; Chen, J.; Deng, J.; Lin, K.; Xing, X.; Negative thermal expansion in molecular materials. *Chem. Commun.*, **2018**, 54, 5164-5176.

(19) Barrera, G. D.; Bruno, J. A. O.; Barron, T. H. K.; Allan, N. L.; Negative thermal expansion. *J. Phys.: Condens. Matter*, **2005**, 17, R217.

(20) Engel, E. R.; Smith, V. J.; Bezuidenhout, C. X.; Barbour, L. J.; Uniaxial negative thermal expansion facilitated by weak host-guest interactions. *Chem. Commun.*, **2014**, 50, 4238-4241.

(21) Attfield, P. J.; Mechanisms and materials for NTE. *Front. Chem.*; **2018**, 6, 371.

(22) Wendt, D.; Bozin, E.; Neuefeind, J.; Page, K.; Ku, W.; Wang, L.; Fultz, B.; Tkachenko, A. V.; Zaliznyak, I. A.; Entropic elasticity and negative thermal expansion in a simple cubic crystal. *Sci. Adv.*; **2019**, 5, eaay2748.

(23) Liu, Z-K.; Wang, Y.; Shang, S.; Thermal expansion anomaly regulated by entropy. *Sci. Rep.*, **2014**, 4, 7043.

(24) Mu, B.; Walton, K. S.; Thermal analysis and heat capacity study of metal-organic frameworks. *J. Phys. Chem. C*, **2011**, 115, 22748-22754.

(25) Szafrański, M.; Katrusiak, A.; Giant Dielectric Anisotropy and Relaxor Ferroelectricity Induced by Proton Transfers in NH$^+$ • • • N-Bonded Supramolecular Aggregates. *J. Phys. Chem. B*, **2008**, 112, 6779-6785.

(26) Hemberger, J.; Lunkenheimer, P.; Fichtl, R.; Krug von Nidda, H.-A.; Tsurkan, V.; Loidl, A.; Relaxor ferroelectricity and colossal magnetocapacitive coupling in ferromagnetic CdCr$_2$S$_4$. *Nature*, **2005**, 434, 364-367.

(27) Wang, D.; Bokov, A. A.; Ye, Z.-G.; Hlinka, J.; Bellaiche, L.; Subterahertz dielectric relaxation in lead-free Ba(Zr,Ti)O$_3$ relaxor ferroelectrics. *Nat. Commun.*, **2016**, 7, 11014.

(28) Tayi, A. S.; Shveyd, A. K.; Sue, A. C. -H.; Szarko, J. M.; Rolczynski, B. S.; Cao, D.; Kennedy, T. J.; Sarjeant, A. A.; Stern, C. L.; Paxton, W. F.; Wu, W.; Dey, S. K.; Fahrenbach, A. C.; Guest, J. R.; Mohseni, H.; Chen, L. X.; Wang, K. L.; Stoddart, J. F.; Stupp, S. I.; Room-temperature ferroelectricity in supramolecular networks of charge-transfer complexes. *Nature,* **2012**, 488, 485-489.

(29) Narayanan, A.; Cao, D.; Frazer, L.; Tayi, A. S.; Blackburn, A. K.; Sue, A. C. -H.; Ketterson, J. B.; Stoddart, J. F.; Stupp, S. I.; Ferroelectric Polarization and Second Harmonic Generation in Supramolecular Cocrystals with Two Axes of Charge-Transfer. *J. Am. Chem. Soc.*, **2017**, 139, 9186-9191.

(30) Wiscons, R. A.; Goud, N. R.; Damron, J. T.; Matzger, A. J.; Room-Temperature Ferroelectricity in an Organic Cocrystal. *Angew. Chem. Int. Ed.*, **2018**, 57, 9044-9047.

(31) Scott, J. C.; Semiconductors and Semimetals: Highly Conducting Quasi One-dimensional Organic Crystals, Academic Press, San Diego, **1988**.

(32) Akutagawa, T.; Nakamura, T.; Inabe, T.; Underhill, A. E.; Structures of Ni(dmit)2 salts of lithium or ammonium included in crown ether assemblies. *Thin Solid Films*, **1998**, 331, 264-271.

(33) Akutagawa, T.; Nakamura, T.; Control of assembly and magnetism of metal-dmit complexes by supramolecular cations. *Coord. Chem. Rev.*, **2002**, 226, 3-9.

(34) Steimecke, G.; Sieler, H.-J.; Kirmse R.; Hoyer, E.; 1.3-DITHIOL-2-THION-4.5-DITHIOLAT AUS SCHWEFELKOHLENSTOFF UND ALKALIMETALL. *Phosphorous Sulfur Relat. Elem.*, **1979**, 7, 49-55.

(35) Czupiński, O.; Jakubas, R.; Pietraszko, A.; On structural phase transitions in 4-aminopyridinium fluoroborate, [4-NH$_2$C$_5$H$_5$N][BF$_4$]: differential scanning calorimetry, dielectric and infrared studies. *J. Mol. Struct.*, **2004**, 704, 177-187.

(36) Sheldrick, G. M.; *SHELXT* - Integrated space-group and crystal-structure determination. *Acta Crystallogr. Sect. A Found. Adv.*, **2015**, 71, 3-8.

(37) Dolomanov, O. V.; Bourhis, L. J.; Gildea, R. J.; Howard, J. A. K.; Puschmann, H.; *OLEX2*: a complete structure solution, refinement and analysis program. *J. Appl. Crystallogr.*, **2009**, 42, 339-341.

(38) Bain G. A.; Berry, J. F.; Diamagnetic Corrections and Pascal's Constants. *J. Chem. Educ.*, **2008**, 85, 532-536.

(39) Mori, T.; Kobayashi, A.; Sasaki, Y.; Kobayashi, H.; Saito, G.; Inokuchi, H.; The Intermolecular Interaction of Tetrathiafulvalene and Bis(ethylenedithio)tetrathiafulvalene in Organic Metals. Calculation of Orbital Overlaps and Models of Energy-band Structures. *Bull. Chem. Soc. Jpn.*, **1984**, 57, 627-633.

(40) Becke, A. D., Density-Functional Thermochemistry. III. The Role of Exact Exchange. *J. Chem. Phys.* **1993**, 98, 5648–5652.

(41) Hehre, W. J.; Ditchfield, R.; Pople, J. A., Self—Consistent Molecular Orbital Methods. XII. Further Extensions of Gaussian—Type Basis Sets for Use in Molecular Orbital Studies of Organic Molecules, *J. Chem. Phys.* **1971**, 56, 2257‑2261.

(42) Grimme, S.; Antony, J.; Ehrlich, S.; Krieg, H.; A consistent and accurate ab initio parametrization of density functional dispersion correction (DFT-D) for the 94 elements H-Pu. *J. Chem. Phys.*, **2010**, 132, 154104.

(43) Gaussian 16, Revision B.01, Frisch, M. J.; Trucks, G. W.; Schlegel, H. B.; Scuseria, G. E.; Robb, M. A.; Cheeseman, J. R.; Scalmani, G.; Barone, V.; Petersson, G. A.; Nakatsuji, H.; Li, X.; Caricato, M.; Marenich, A. V.; Bloino, J.; Janesko, B. G., Gomperts, R.; Mennucci, B.; Hratchian, H. P.; Ortiz, J. V.; Izmaylov, A.F.; Sonnenberg, J.L.; Williams-Young, D.; Ding, F.; Lipparini, F.; Egidi, F.; Goings, J.; Peng, B.; Petrone, A.; Henderson, T.; Ranasinghe, D.; Zakrzewski, V.G., Gao, J., Rega, N., Zheng, G., Liang, W., Hada, M., Ehara, M., Toyota, K., Fukuda, R., Hasegawa, J., Ishida, M., Nakajima, T., Honda, Y., Kitao, O., Nakai, H., Vreven, T., Throssell, K.,

Montgomery Jr., J.A., Peralta, J.E., Ogliaro, F., Bearpark, M.J., Heyd, J.J., Brothers, E.N., Kudin, K.N., Staroverov, V.N., Keith, T.A., Kobayashi, R., Normand, J., Raghavachari, K., Rendell, A.P., Burant, J.C., Iyengar, S.S., Tomasi, J., Cossi, M., Millam, J.M., Klene, M., Adamo, C., Cammi, R., Ochterski, J.W., Martin, R.L., Morokuma, K., Farkas, O., Foresman, J.B., Fox, D.J. Gaussian, Inc., Wallingford CT, **2016**

For Table of Contents Only